Influence of Operating Parameters on the Ballistics of a Lab-Scale Vortex Flow Pancake Hybrid Rocket Engine

Christian Paravan, Federico Piscaglia, and Luciano Galfetti
Politecnico di Milano, Aerospace Science and Technology Dept.,
Space Propulsion Laboratory (SPLab),
34, via LaMasa, 20156, Milan, Italy

Abstract

Cold-flow visualizations and combustion tests are performed in a lab-scale vortex flow pancake (VFP) hybrid rocket engine. The characterization aims at providing an insight of the operating parameters influence on the VFP motor behavior. The main observables of interests are the solid fuel regression rate (r_f) and the characteristic velocity combustion efficiency (η_{c*}). Under the investigated conditions the combustion of hydroxyl-terminated polybutadiene (HTPB) and gaseous O_2 exhibits r_f dependence on total mass flux. The η_{c*} shows values in the range 90-99% thanks to the vortex flow.

1. Introduction

Hybrid rocket engines (HREs) are thermochemical propulsion systems featuring oxidizer and fuel in different states of matter. This configuration offers attractive features as high theoretical specific impulse (I_s), operating flexibility (i.e., multiple ignitions, thrust throttling), and high safety levels (in turn yielding recurring cost reduction thanks to the easy manufacturing and transportation of the motor) [1]. The implementation of HREs has been so far hampered by their intrinsically low regression rate (r_f) and poor combustion efficiency.

This paper discusses an innovative motor configuration: the vortex flow pancake (VFP) [2][3]. In this non-conventional motor geometry, a tangential oxidizer injector is sandwiched between two fuel disks. One of the disks features a central port connecting the combustion chamber to the exhaust nozzle. With this implementation large surface areas can be achieved with a simple design and with a combustion chamber length-to-diameter ratio (L/D) < 1. The tangential injection of the oxidizer induces a vortex flow-field between two solid fuel disks. Hence, the mixing between fuel and oxidizer is enhanced, leading to possible combustion efficiency enhancements. The VFP considered in the study was designed, implemented and tested at the Space Propulsion Laboratory (SPLab) of Politecnico di Milano [3].

1.1 Literature Survey

In a HRE the solid fuel pyrolysis products react with the atomized/gaseous oxidizer flow in a turbulent boundary layer. This diffusion-limited phenomenon was the object of intense studies during the 1960s, that were recently extended [1][4-8]. The turbulent boundary layer combustion of polymeric fuels in standard flow configurations was investigated by Marxman and co-workers [4-6]. In these analyses, convective heat transfer was considered as the main input driving the solid fuel vaporization. Therefore, the total mass flux (G) was identified as the main controlling parameter for the solid fuel regression, $r_f \sim G(x)^{0.8}$. The convective heat transfer process is hindered by the mass blowing effect from the condensed phase. Thus, the effective heat transfer coefficient is reduced during burning [4-6]. This causes the intrinsic r_f limitation characterizing the HRE combustion process. The turbulent boundary layer combustion model based on the solid fuel gasification has been recently extended for liquefying fuel formulations granting enhanced r_f[7,8]. While showing attractive performance for the design of high-thrust systems, the fuels producing entrainment (i.e., cryogenic hybrids, solid paraffin waxes) exhibit poor mechanical properties (or complex implementation) hindering their possible applications in affordable operating systems. The r_f enhancement (crucial for the application of HRE to high-thrust missions), is currently pursued by different approaches as solid fuel loading with energetic additives [9-10], and exotic oxidizer injection techniques [11-15].

Non-conventional injection techniques and exotic grain configurations may yield augmented performance in terms of solid fuel r_f and combustion efficiency by increasing flow turbulence. The two approaches may be joined [1]. In exotic injection techniques applied to conventional motor configurations (cylindrical grains with length-to-diameter-ratio, $L/D > 1$), the oxidizer inlet configuration promotes a vortex flow whose effects are heat transfer enhancement (thanks to the augmented parallel and tangential velocity components), improved propellant mixture mixing and residence time. This technique enables r_f enhancement over standard oxidizer injection up to 270% [11]. On the other hand, for systems of relatively large size (i.e., grain length) this technique implies some intrinsic limitation due to the tangential

velocity component loss induced by viscous dumping and mass blowing [15]. This effect can be lessened by helical/tapered fuel grain configurations [13,14], and by the implementation of multiple injectors along the fuel grain [15]. Exotic vortex flow HRE configurations were proposed by Gibbon et al. [2], Knuth et al. [12], and Rice et al. [16]. The VFP motor configuration described in [2] yields a compact HRE implementation (large fuel gasification surface area can be achieved by increasing the combustion chamber diameter, and not the engine length). These configurations feature increased r_f with respect to the conventional implementations burning under similar G [2, 3, 12, 16]. Detailed numerical analyses on the internal flow-field of vortex-flow HRE are discussed by Majdalani in [17] and in Refs. 3, 18.

2. The SPLab Vortex Flow Pancake

The SPLab VFP (SVFP) is shown in Figure 1 [3]. Two opposite fuel disks are faced to the injector ring and limit the combustion chamber volume. Injection is performed by four tangential (and equally spaced) inlets placed on the lateral surface of the combustion chamber. Both the fuel disks exhibit a donut-like shape, with central port perforations. One of these ports enables the flow of combustion products toward the nozzle, while the other is used to inject the N_2 purge for the combustion interruption. The system is completed by two flanges. One of them is connected to the water-cooled nozzle, while the other lodges the igniter. Both flanges enable the integration of sensors (e.g., thermocouples, wire-cut r_f sensors).The system is ignited by a pyrotechnic primer charge. The combustion chamber pressure (p_c) is measured by a piezo-resistive pressure transducer, while the oxidizer mass flow rate ($\dot{m}_{ox}$) is monitored by a digital flowmeter. The two fuel disks of the SVFP are identified as nozzle-side grain (top of the Figure 1b), and nitrogen-side grain (bottom of the Figure 1b). The combustion chamber height (H_{cc}) of the motor is defined as the separation between the two fuel disks.

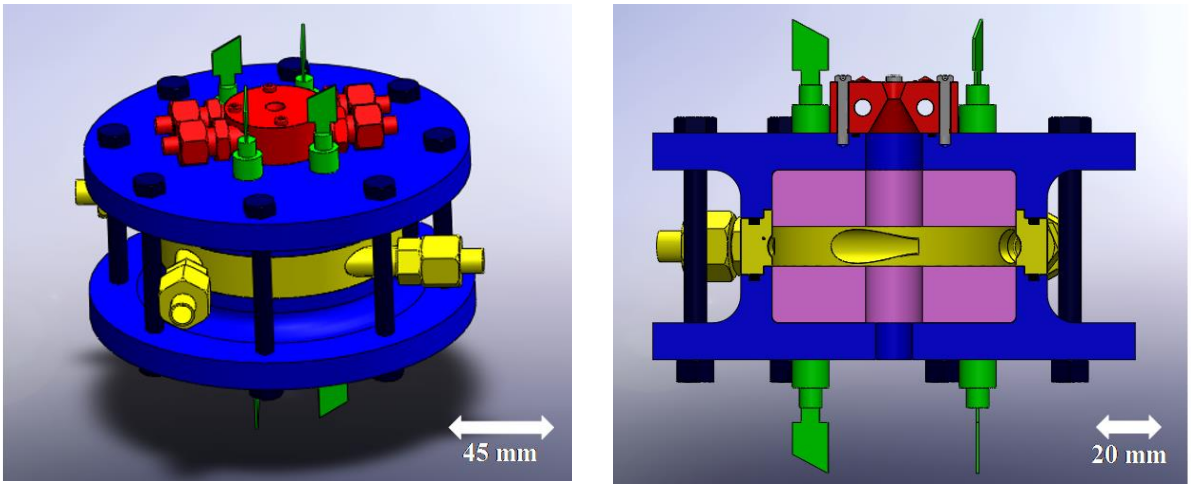

a **b**

Figure 1: Overview of the SPLab VFP configuration (a) external and (b) cross section views: flanges and fuel grain holders (blue), injection ring (yellow), solid fuel grain (violet), water-cooled nozzle (red), and sensors (green).

3. The SPLab VFP Internal Flow-field

The internal flow-field of the SVFP is investigated by cold-flow experiments performed on a purposely implemented transparent SVFP mock-up. The high-speed visualizations are performed at 1000 fps, with air as a carrier, and 1,2-propandiol smoke as tracer. The tests are performed with p_c of 0.2 MPa and $\dot{m}_{ox}$ of 0.25 and 0.50 g/s. The combustion chamber pressure limitation is due to the thickness of the transparent SVFP flanges, that are realized in Plexiglas, while the $\dot{m}_{ox}$ range is selected to grant good flow insemination by the tracer.

Visualization tests are performed recording the internal flow-field view by the (transparent) nitrogen-side flange. Different combustion chamber heights (representing different separations between the fuel disks) are considered in the analysis. The aim is an insight of the SVFP vortex flow differences induced by the internal configuration of the motor.

Image sequences captured at H_{cc} = 20 mm (ignition of the SVFP) and at H_{cc} = 60 mm (fuel grains burnout) are shown in Figure 2 and in Figure 3 respectively. Focusing on the image sequence of Figure 2, the effect of $\dot{m}_{ox}$ on the vortex structure is evident. Increasing the oxidizer mass flow rate (thus, the inlet velocity), the flow streamlines appear more regular and uniform. The H_{cc} increase reduces the uniformity of the vortex, yielding a 3D structure due to the reduced oxidizer flow velocity. The reduced intensity of the vortex flow due to the combustion chamber height increase could imply a reduction in the motor efficiency due to the less intense mixing of the reacting propellant.

The Figure 4 shows the internal flow-field of the SVFP as captured by a CFD simulation performed by OpenFOAM. The numerical simulation is performed considering a $\dot{m}_{ox}$ = 10 g/s and H_{cc} = 20 mm, but the overall structure of the velocity field shows a good agreement with the minimum combustion chamber height visualizations in the Figure 1, and with those reported in the Ref. 3.

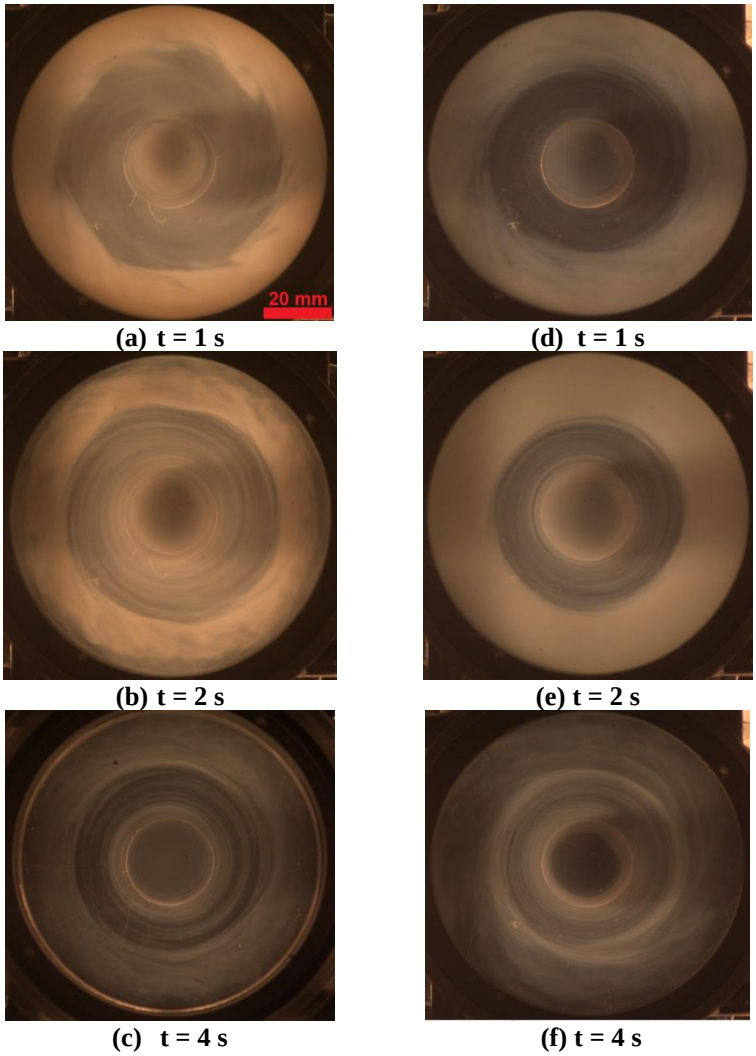

Figure 2: Internal flow-field visualization of the SVFP (N_2-side flange, H_{cc} = 20 mm): (a-c) $\dot{m}_{ox}$ = 0.25 g/s, (d-f) $\dot{m}_{ox}$ = 0.5 g/s.

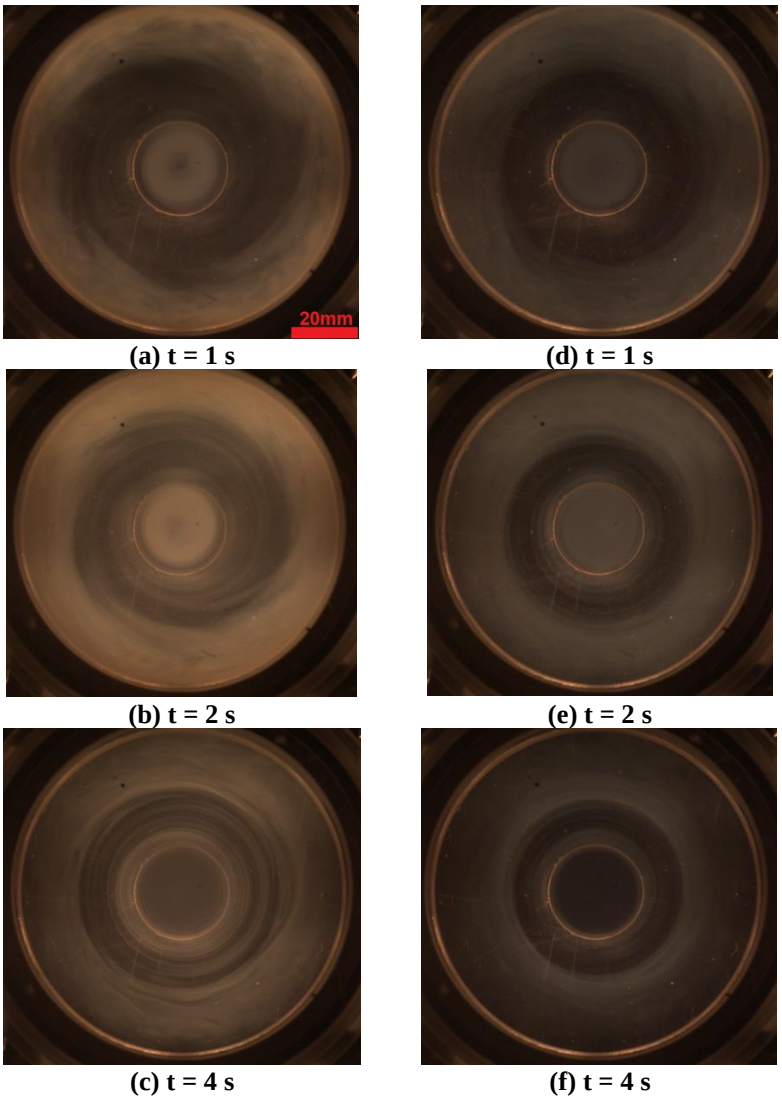

Figure 3: Internal flow-field visualization of the SVFP (N_2-side flange, H_{cc} = 60 mm): (a-c) $\dot{m}_{ox}$ = 0.25 g/s, (d-f) $\dot{m}_{ox}$ = 0.50 g/s.

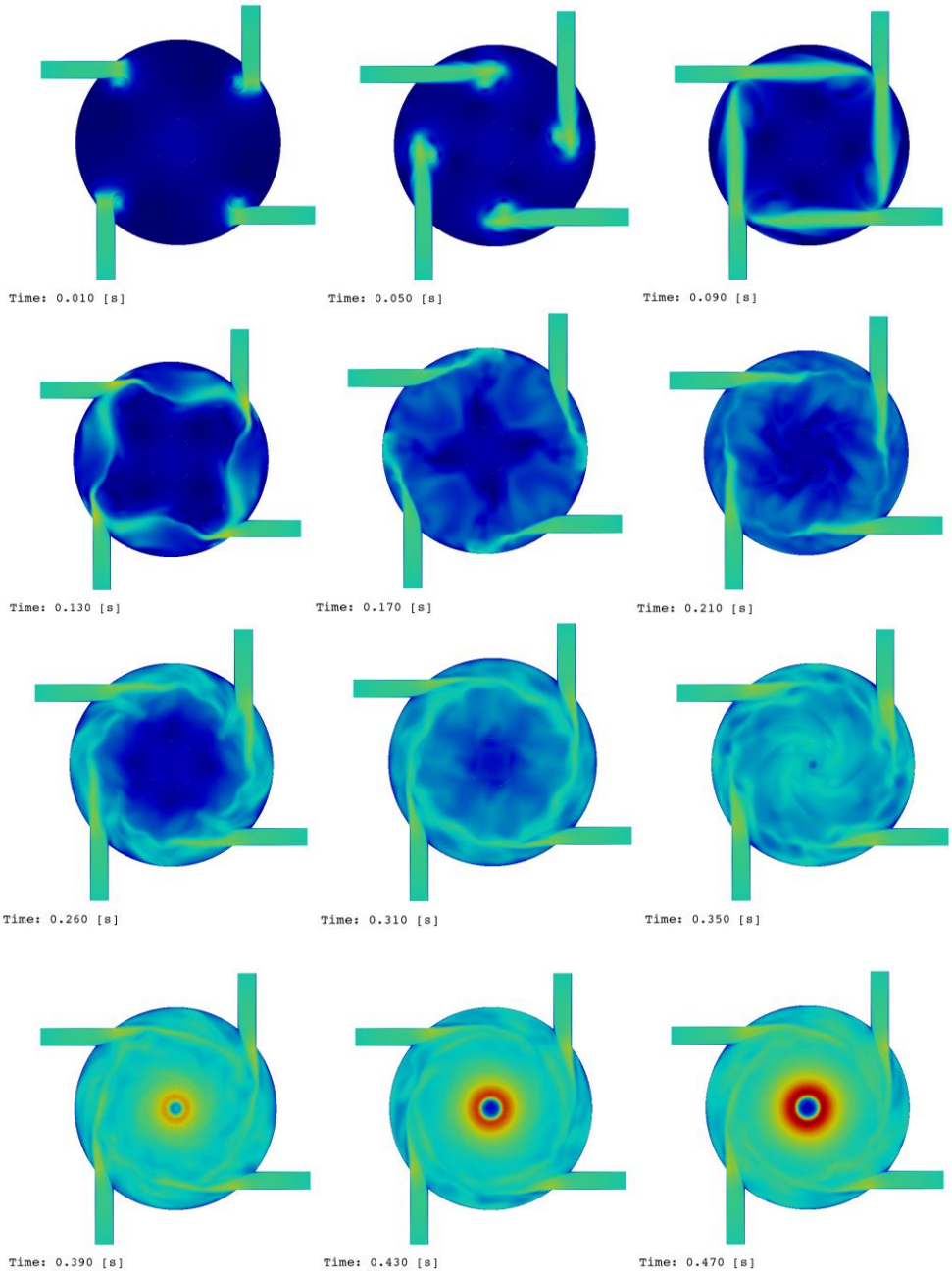

Figure 4: CFD simulation of the internal flow-field of the SVFP for $\dot{m}_{ox}$ = 10 g/s and H_{cc} = 20 mm: velocity evolution in time [18].

3. Combustion Experiments

The SVFP burning behavior is investigated considering hydroxyl-terminated polybutadiene (HTPB) as fuel, and gaseous O_2 (GOX) as oxidizer. The HTPB features a curing level ([-NCO]/[-OH]) of 1.04. The fuel formulation is based on HTPB R45 (79.2 wt.%), dioctyl-adipate (DOA, 13.1 wt.%) and isophorone diisocyanate (IPDI, 7.7 wt.%) [18,21]. The same couple of fuel grains is burnt in a series of combustion runs of variable duration.

3.1 Regression Rate and Combustion Efficiency Data Reduction

The burning behavior of the SVFP is investigated focusing on two main observables of interest: the solid fuel regression rate and the combustion efficiency based on the characteristic velocity (η_{c*}). The solid fuel regression rate is evaluated by thickness over time (TOT) and time-resolved techniques. The TOT method is implemented in two variants, both based on the combustion chamber pressure history in time. The direct measurement of the solid fuel

grain thickness is the simplest and widest used technique for the fuel consumption determination. The second TOT method is a mass balance-based technique. The use of the mass-based TOT requires the definition of the solid fuel grain burning area (A_b) and of the solid fuel density (ρ_f). From these data, the fuel mass change due to combustion (Δm_f) and the burning time (Δt_b) yield to the space- and time-averaged r_f ($\langle \bar{r}_f \rangle$) as

$$\langle \bar{r}_f \rangle = \frac{\Delta m_f}{\rho_f A_b \Delta t_b} \tag{1}$$

The burning time is defined thanks to the pressure history in time. Figure 5 shows typical $p_c(t)$ history during a SVFP combustion test. The burning time is assumed to start when the instantaneous $p_c(t)$ reaches the 70% of the maximum value characterizing the burning phase, and extends till GOX is stopped to let the nitrogen purge in. The space- and time-averaged oxidizer mass flux ($\langle \bar{G}_{ox} \rangle$) and total mass flux ($\langle \bar{G}_{tot} \rangle$) are evaluated considering the operating conditions ($\dot{m}_{ox}$), the fuel mass regression rate ($\overline{\dot{m}_f} = \Delta m / \Delta t_b$), and the space- and time-averaged combustion chamber height ($\langle \bar{H}_{cc} \rangle$) and radius ($R_{cc}$). The $\langle \bar{H}_{cc} \rangle$ is defined measuring the combustion chamber height before and after the firing test, and averaging the two values.

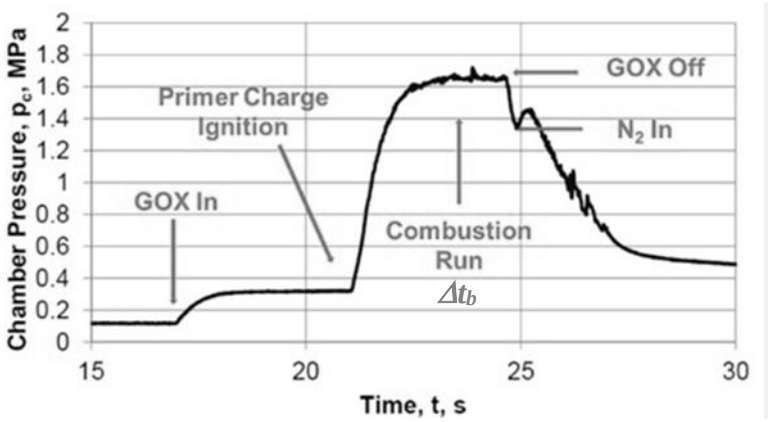

Figure 5: Typical $p_c(t)$ history of a SVFP combustion run.

Independently from the technique implemented for the r_f determination, the SVFP combustion efficiency (η_{c*}) of the performed combustion tests is evaluated considering the actual and the theoretical characteristic velocity (c^*) values. The former is evaluated by the average chamber pressure of the run

$$\bar{p}_c = \frac{1}{\Delta t_b} \int_{\Delta t_b} p_c(t) dt \tag{2}$$

and by the time-averaged overall mass flow rate ($\overline{\dot{m}_f}$). The theoretical c^* is determined based on the experimental oxidizer-to-fuel ratio (O/F) and $\bar{p}_c$ by the NASA CEA code [22,23].

3.2 Experimental Results

Experimental results are hereby presented and discussed. The comparison between the two implemented TOT techniques (grain thickness and mass-balance) is introduced first. These combustion runs are performed under special operating conditions ($\dot{m}_{ox}$ = 4 g/s, initial H_{cc} ~35 mm). Then, a detailed analysis of the burning behaviour of the SVFP is given considering 2 g/s ≤ $\dot{m}_{ox}$ ≤ 8 g/s with initial H_{cc} ~20 mm.

Experimental results contrasting TOT results obtained by grain thickness and mass balance measurements are reported in the Table 1. The test H1 is divided into two runs (H1-R1, and H2-R2 respectively). In the first run, the initial combustion chamber height ($\overline{\langle H_{cc,ini} \rangle}$) is 36.4 ± 0.2 mm. In the two runs, the $\langle \bar{H}_{cc} \rangle$ resulting from the direct measurement of the fuel grain thickness is 38.3 ± 0.2 mm and 41.9 ± 0.2 mm respectively. These data are consistent with the $\langle \bar{H}_{cc} \rangle$ values calculated from $r_{f,TH}$ and Δt_b as

$$\overline{\langle H_{cc} \rangle} = \overline{\langle H_{cc,ini} \rangle} + \overline{\langle r_{f,TH} \rangle} \Delta t_b \tag{3}$$

The TOT data reduced by the grain thickness measurement show a good agreement with the data based on the mass balance (MB) method, so do the $\langle \bar{H}_{cc} \rangle$ calculated from the ballistic data retrieved from the same technique. These considerations hold for the second test, H2, that is divided into three runs (see Table 1). The SVFP feature thermal protections in the ports of the fuel grain. This is done to prevent a non-uniform grain consumption while protecting the metal case of the motor (and the combustion chamber-nozzle coupling). The good agreement between the solid fuel grain thickness data, and the mass balance-derived parameters testifies the absence of marked effects on the $r_{f,MB}$ and $G_{tot,MB}$ of the thermal protection consumption. In light of this, only MB data will be considered in the following analyses. The tests reported in Table 1 and Table 2 show a decreasing $r_f(G_{tot})$ trend. The power law approximation of the $\overline{\langle r_f \rangle}$ as a function of $\langle \overline{G_{tot}} \rangle$ yields:

$$\overline{\langle r_f \rangle} = 0.064 \langle \overline{G_{tot}} \rangle^{1.20}, R^2 = 0.96 \quad (4)$$

The high exponent of the total mass flux is probably related to the limited number of points available, and to the restricted G_{tot} range (see Table 1).
Under the investigated conditions, the η_{c*} of the SVFP is in the range 89-90% (see Table 2). These relatively low values are probably related to the reduced $\dot{m}_{ox}$, and to the relatively high $\langle \bar{H}_{cc} \rangle$, in turn implying reduced G_{tot} and, thus, a limited vortex intensity. On the other hand, it should be noted that the system does not feature any post-combustion chamber, thus, the achieved c^* efficiency is due to the oxidizer vortex injection alone. An overview of the burning tests performed on the SVFP is reported in the Table 3. Collected data show a decreasing trend of the r_f for increasing $\langle \bar{H}_{cc} \rangle$ and decreasing $\langle \bar{G}_{ox} \rangle$ (and $\langle \bar{G}_{tot} \rangle$). A power law interpolation of $\overline{\langle r_f \rangle}(\langle \overline{G_{tot}} \rangle)$ yields:

$$\overline{\langle r_f \rangle} = 0.061 \langle \overline{G_{tot}} \rangle^{0.85}, R^2 = 0.87 \quad (5)$$

Table 1: TOT results from direct fuel grain measurement ($G_{tot,th}$, $r_{f,th}$) and mass-balance ($G_{tot,MB}$, $r_{f,MB}$). Tests performed in GOX, with $\dot{m}_{ox}$ = 4 g/s.

Test id.	$\overline{p_c}$, MPa	Δt_b, s	$\langle \overline{G_{tot,th}} \rangle$, kg/m²s	$\overline{\langle r_{f,th} \rangle}$, mm/s	$\langle \overline{G_{tot,MB}} \rangle$, kg/m²s	$\overline{\langle r_{f,MB} \rangle}$, mm/s
H1-R1	0.78	9.5	3.73	0.21 ± 0.01	3.76	0.21 ± 0.01
H1-R2	0.74	9.4	3.24	0.18 ± 0.01	3.32	0.19 ± 0.01
H2-R1	0.78	8.8	4.09	0.22 ± 0.02	4.23	0.24 ± 0.01
H2-R2	0.71	9.7	3.61	0.20 ± 0.02	3.61	0.20 ± 0.01
H2-R3	0.68	10.1	3.05	0.16 ± 0.01	3.08	0.16 ± 0.01

Table 2: relevant data from MB ballistics for tests H1 and H2 ($\dot{m}_{ox}$ = 4 g/s).

Test id.	$\overline{p_c}$, MPa	Δt_b, s	$\langle \overline{O/F} \rangle$,	η_{c*},%
H1-R1	0.78	9.5	1.8	90
H1-R2	0.74	9.4	2.0	90
H2-R1	0.78	8.8	1.6	89
H2-R2	0.71	9.7	1.8	89
H2-R3	0.68	10.1	2.4	89

In the Eq. 5 the $\langle \overline{G_{tot}} \rangle$ exponent takes a relatively high value, possibly due to the different intensity of the vortex flow at the two investigated mass flow rates. The $\overline{\langle r_f \rangle}(\langle \overline{G_{tot}} \rangle)$ is similar to the one achieved by HTPB + GOX burning in conventional configurations [1]. The combustion of the SVFP is driven by the convective heat transfer, with some possible contribution from radiation (due to the formation of soot, see O/F values in Table 2). The vortex flow enables effective mixing of the propellant mixture, as testified by the η_{c*} values reported in the Table 3. The combustion efficiency shows a decreasing trend for increasing combustion chamber height. This is mainly related to the loss of intensity of the vortex flow [3]. Regression rate differences noted between data reported in Table 1 and experimental results in the Table 3 requires further investigations to clarify the nature of the difference.

In the Table 3, the parameter Φ is introduced. This is a non-dimensional ratio providing an indication of the symmetry of the combustion chamber. In particular, Φ is defined as the ratio of the distances from the symmetry plane of the combustion chamber of the surfaces of the N_2-side and of the nozzle-side fuel grains. This symmetry index shows a decreasing trend during the burnings of a series (see Table 3). This is due to the different burning rate achieved by the two fuel disks, with the nozzle-side grain exhibiting higher r_f than the N_2-side counterpart. This behavior is related to the internal flow-field of the SVFP [3]. The different regression rates of the two fuel disks of the SVFP are shown in

the Table 4. On average, the r_f percent difference between the r_f of the two fuel grains is the 40% of the overall $r_{f,MB}$ characterizing the tests.

Table 3: Relevant ballistic data for SVFP burning in GOX, with 4 g/s ≤ $\dot{m}_{ox}$ ≤ 8 g/s (data reduction by MB). For all the tests, the initial run is performed starting from $H_{cc,ini}$ = 20 ± 1.0 mm.

Test id.	$\overline{p_c}$, MPa	Δt_b, s	$\dot{m}_{ox}$, g/s	$\langle \overline{G_{tot}} \rangle$, kg/m²s	$\overline{\langle r_f \rangle}$, mm/s	η_{c*}, %	$\overline{\langle \Phi \rangle}$
H3-R1	0.46	8.80	2	3.73	0.134 ± 0.002	99	0.98
H3-R2	0.43	23.0	2	3.28	0.159 ± 0.002	93	0.92
H3-R3	0.43	11.2	2	2.69	0.156 ± 0.002	92	0.85
H3-R4	0.41	9.70	2	2.34	0.141 ± 0.002	90	0.83
H3-R5	0.74	9.80	4	3.74	0.200 ± 0.006	88	0.81
H4-R1	1.70	16.8	8	9.64	0.433 ± 0.002	97	0.92
H4-R2	1.46	15.7	8	6.20	0.321 ± 0.002	95	0.83

Table 4: Regression rate of nozzle- and N_2-side grains for SVFP burning in GOX, with 4 g/s ≤ $\dot{m}_{ox}$ ≤ 8 g/s (data reduction by MB). For all the tests, the initial run is performed starting from $H_{cc,ini}$ = 20 ± 1.0 mm.

Test id.	$\overline{\langle r_f \rangle}$, mm/s	$\overline{\langle r_{f,N2} \rangle}$, mm/s	$\overline{\langle r_{f,Nozzle} \rangle}$, mm/s
H3-R1	0.134 ± 0.002	0.113 ± 0.002	0.155 ± 0.002
H3-R2	0.159 ± 0.002	0.121 ± 0.002	0.197 ± 0.002
H3-R3	0.156 ± 0.002	0.122 ± 0.002	0.191 ± 0.002
H3-R4	0.141 ± 0.002	0.112 ± 0.002	0.171 ± 0.002
H3-R5	0.200 ± 0.006	0.156 ± 0.006	0.245 ± 0.006
H4-R1	0.433 ± 0.002	0.350 ± 0.002	0.517 ± 0.002
H4-R2	0.321 ± 0.002	0.249 ± 0.002	0.392 ± 0.002

4. Conclusions and Future Developments

This paper discusses the ongoing SPLab activities on the investigation of a lab-scale HRE with a VFP configuration (see Figure 1). This motor promises high *c** combustion efficiencies thanks to the vortex combustion. This, together with the attractive features of the VFP configuration (compactness, easy implementation on different platforms) could yield an effective use of HRE for in-space applications. The internal flow-field of the motor was investigated by high-speed visualizations (see Figure 2 and Figure 3) and CFD analyses [3, 18]. The burning behavior of the SVFP was investigated burning HTPB + GOX with 4 g/s ≤ $\dot{m}_{ox}$ ≤ 8 g/s, in turn yielding 2.3 kg/(m²s) ≤ $\overline{\langle G_{tot} \rangle}$ ≤ 9.6 kg/(m²s). In spite of the relatively low mass flux conditions, the SVFP exhibited a convection-driven combustion (see Eq. 5). The two fuel disks show different regression rates, with a faster nozzle-side grain. The η_{c*} of the motor is in the range 88% to 99% and is related to the intensity of the vortex flow, though under the investigated conditions, a possible effect of the combustion chamber symmetry is noted for low $\dot{m}_{ox}$ conditions.

The achieved results show promising perspectives in the implementation of a hybrid propulsion-based platform enabling efficient and affordable performance and operating flexibility. Future developments of the work will focus on the expansion evaluation of the η_{c*} for different levels of the combustion chamber symmetry parameter Φ, and on the measurement of the SVFP thrust and related parameters (as the specific impulse).

References

[1] Chiaverini, M.J. 2007. Review of Solid Fuel Regression Rate Behavior in Classical and Non-classical Hybrid Rocket Motors. In: *Fundamentals of Hybrid Rocket Combustion and Propulsion*, edited by M.J. Chiaverini and K.K. Kuo, Progress in Astronautics and Aeronautics, AIAA, Washington, DC, 2007, Chapter 2, pp. 37–125.

[2] Gibbon, D. M., and Haag G.S. 2001. Investigation of an Alternative Geometry Hybrid Rocket for Small Spacecraft Orbit Transfer. *DTIC Technical Report*, AD No. 393398, 2001.

[3] Paravan, C., Glowacki, J., Carlotti, S., Maggi, F., and Galfetti, L. 2016. Vortex Combustion in a Lab-Scale Hybrid Rocket Motor. *AIAA Paper No. 2016-4562*.

[4] Marxman, G.A., and Gilbert, M. 1963. Turbulent Boundary Layer Combustion in the Hybrid Rocket. In: *9th International Symposium on Combustion*, Academic Press, Inc., New York, pp. 371-383.

[5] Marxman, G.A. 1967. Boundary Layer Combustion in Propulsion. In: *Proceedings of the 11th Symposium (International) on Combustion*, The Combustion Institute, Pittsburg, Pennsylvania, pp. 269-289.
[6] Marxman, G.A., and Wooldridge, C.E. 1968. "Research on the Combustion Mechanism of Hybrid Rockets," *Advances in Tactical Rocket Propulsion*, Edited by S.S. Penner, AGARD Conference Proceedings No. 1, pp. 421-477.
[7] Karabeyoglu, M.A., Altman, D., and Cantwell, B.J. 2002. Combustion of Liquefying Hybrid Propellants: Part 1, General Theory. *J. Prop. Power*, Vol.18, No. 3, pp. 610-620.
[8] Karabeyoglu, M.A., and Cantwell, B.J. 2002. Combustion of Liquefying Hybrid Propellants: Part 2, Stability of Liquid Films. *J. Prop. Power*, Vol.18, No. 3, pp. 621-630.
[9] Risha, G.A., Evans, B.J., Boyer, E., and Kuo, K.K. 2007. Metals, Energetic Additives and Special Binders Used in Solid Fuels for Hybrid Rockets. In: *Fundamentals of Hybrid Rocket Combustion and Propulsion*, edited by M.J. Chiaverini, and K.K. Kuo, Progress in Astronautics and Aeronautics, AIAA, Washington, DC, Chapter 10, pp. 413–456.
[10] Paravan, C. 2012. Ballistics of Innovative Solid Fuel Formulations for Hybrid Rocket Engines. Ph.D. Dissertation, Dept. of Aerospace Science and Technology, Politecnico di Milano, Milan, Italy.
[11] Yuasa, S., Shimada, O., Imamura, T., Tamura, T., and Yamamoto, K. 1999. A Technique for Improving the Performance of Hybrid Rocket Engines. *AIAA Paper No. 99-2322*.
[12] Knuth, W.A., Chiaverini, M.J., Sauer, J.A., and Gramer, D.J. 2002.Solid–fuel Regression Rate Behavior of Vortex Hybrid Rocket Engines. *J. Propul. Power*, Vol.18, No. 3, pp. 600-609.
[13] Lee, C., Na,Y., and Lee, G. 2005. The Enhancement of Regression Rate of Hybrid Rocket Fuel by Helical Grain Configuration and Swirl Flow. *AIAA Paper 2005-3906.*
[14] Wilkinson, R., Hart, K., Day, R., and Coxhill, I. 2010. Proof-of-Concept Testing of a Sustained Vortex-Flow Configuration for Hybrid Rocket Motors. *AIAA Paper No. 2010-6782*.
[15] Ohyama, S., Aso, S., Hirata, Y., Araki, K., Ohe, K., Tani, Y., and Shimada, T. 2012. A Study of Hybrid Rocket Engine with Multi-Section Swirl Injection Method. *AIAA Paper No. 2012-3905*.
[16] Rice, E. E., Gramer, D. J., St. Clair, C. P., and Chiaverini, M. J. 2003. "Mars ISRU CO/O2 Rocket Engine Development and Testing. In: *7th NASA International Microgravity Combustion Symposium*, NASA/CP—2003-212376.
[17] Majdalani, J. 2007. Vortex-injection Hybrid Rockets. In: *Fundamentals of Hybrid Rocket Combustion and Propulsion*, edited by M.J. Chiaverini, and K.K. Kuo, Progress in Astronautics and Aeronautics, AIAA, Washington, DC, Chapter 10, pp. 247-276.
[18] Paravan, C., Bisin, R., Piscaglia, F., and Galfetti, L. 2019. Combustion Processes in Hybrid Rockets. *Int. J. Energ. Mat. Chem. Prop.*, accepted for publication.
[19] Barton, I. 1998. Comparison of Simple- and PISO-type Algorithms for Transient Flows. *Int. J. Numer. Methods Fluids*, Vol. 26, No. 4, pp. 459-483.
[20] Boiocchi, M., Paravan, C., Dossi, S., Maggi, F., Colombo, G., and Galfetti, L. 2015. Paraffin-based Fuels and Energetic Additives for Hybrid Rocket Propulsion. *AIAA Paper No. 2015-4042.*
[21] Paravan, C., Manzoni, M., Rambaldi, G., and DeLuca, L.T. 2013. Analysis of Quasi-steady and Forced Transient Burning of Hybrid Solid Fuels in a Laboratory-scale Burner by an Optical Technique. *Int. J. Energ. Mat. Chem. Prop.*, Vol. 12, Issue 5, pp. 385-420.
[22] NASA, CEA: Chemical Equilibrium with Applications, http://www.grc.nasa.gov/WWW/CEAWeb/.
[23] Gordon, S. and McBride, B.J. 1994. Computer Program for Calculation of Complex Chemical Equilibrium Compositions and Applications, NASA Reference Publication, RP-1311.